CHEMICAL PHYSICS

Scattering of adiabatically aligned molecules by nonresonant optical standing waves

Lee Yeong Kim[1]*, Byung Gwun Jin[2]*, Tae Woo Kim[2], Ju Hyeon Lee[2], Bum Suk Zhao[1,2]†

We study the effect of rotational state–dependent alignment in the scattering of molecules by optical fields. CS_2 molecules in their lowest few rotational states are adiabatically aligned and transversely accelerated by a nonresonant optical standing wave. The width of the measured transverse velocity distribution increases to 160 m/s with the field intensity, while its central peak position moves from 10 to −10 m/s. These changes are well reproduced by numerical simulations based on the rotational state–dependent alignment but cannot be modeled when ignoring these effects. Moreover, the molecular scattering by an off-resonant optical field amounts to manipulating the translational motion of molecules in a rotational state–specific way. Conversely, our results demonstrate that scattering from a nonresonant optical standing wave is a viable method for rotational state selection of nonpolar molecules.

INTRODUCTION

Molecular alignment by nonresonant laser fields has been studied extensively for the past three decades (1, 2). Alignment or orientation of molecules is critical for investigations of structural aspects and has been exploited in various experiments including x-ray (3) or electron diffraction in the gas phase (4), generation of high harmonics (5), or tomographic reconstruction of molecular orbitals (6). Molecular alignment also plays a key role when controlling molecular translation with laser fields (7–9).

Alignment occurs through the state-dependent interaction of nonspherical molecules with laser fields, which creates directional states via hybridization of molecular rotation (10). As a result, for instance for linear molecules, the molecular axis becomes aligned along the laser polarization direction. The initially freely rotating molecules are confined and librate angularly around the laser polarization axis without dissipation of the rotational energy. Therefore, the molecules are more tightly angularly confined when their initial rotational energy is small or the laser intensity is large. Namely, the degree of alignment of a given directional state depends on the rotational state associated with it and on the laser intensity. The state-dependent molecular alignment and its coupling to translation are instrumental in determining the motion of molecules in laser fields (10–16). However, so far, experimental results have been interpreted without considering the effects of molecular alignment (17–21). Only recently have the state-averaged alignment effects and the state-dependent interaction been demonstrated for CS_2 molecules in propagating laser fields (7, 8) and standing waves (22), respectively. A low rotational temperature $T_{rot} \sim 35$ K of the molecules played a crucial role in both experiments. Nonetheless, state-dependent alignment was not considered in these experiments. A subsequent theoretical study predicted that scattering of CS_2 molecules at $T_{rot} \sim 1$ K by an optical standing wave would exhibit strong state-dependent alignment effects on the molecular trajectories (23). The present study experimentally confirms this theoretical prediction.

An optical standing wave is created by two counter-propagating laser beams of wavelength λ and amounts to a periodic structure with period λ/2. A matter-wave diffracted from the periodic structure exhibits diffraction peaks separated by integer multiples of $2\hbar\mathbf{k}$ in momentum space, with $\mathbf{k}$ and $-\mathbf{k}$ the wave vectors of the two laser beams and $k = 2\pi/\lambda$. This matter-wave diffraction is known as Kapitza-Dirac (KD) diffraction (24) and was first demonstrated for point-like particles such as atoms (25) and electrons (26). The scattering can also be understood as a deflection of particles by their interaction potential with an optical standing wave. The spatial gradient of the potential imparts a force to the particles, as a result of which their velocities vary after passing through the standing wave. For manipulating atoms, a dipolar interaction potential between the standing wave and the induced dipole moment of the atoms was applied and used to measure polarizabilities (27), and an accelerating, periodic, dipolar potential was used to accelerate metastable Ar atoms from 0 to 200 m/s (28).

Both the coherent and incoherent scattering has been extended to molecules. For large molecules such as C_{60} and C_{70} (29), the coherent KD effect has been explored in a Talbot-Lau interferometer (30). The Talbot-Lau interferometer with KD diffraction then served as an analytical tool to pinpoint the process where molecular fragmentation occurs in a mass spectrometer (31) and to measure the electronic properties of molecules (32). On the other hand, the classical dynamics of small molecules in standing waves has been studied to tailor the translational motions of molecules in a supersonic beam. For instance, standing waves were used to change the longitudinal or transverse velocity distributions of H_2 molecules (33) and CS_2 molecules (22), respectively, by aligning the standing wave parallel or perpendicular to the molecular beam axis.

When the frequencies of the two laser beams creating a standing wave differ by Δω, the standing wave moves with velocity $v_{sw} = \Delta\omega/k$ (34–36). Slow NO molecules (37) and stationary C_6H_6 molecules (38) were produced by the incoherent molecular scattering from a standing wave moving at constant velocity along the molecular beam direction. However, in these extensions of coherent or incoherent KD scattering to molecules, the effects of molecular rotation remained largely unresolved. And yet, it is the molecular rotation, in addition to vibration, that distinguishes molecules from atoms or subatomic particles.

[1]Department of Physics, Ulsan National Institute of Science and Technology, Ulsan, Korea. [2]Department of Chemistry, Ulsan National Institute of Science and Technology, Ulsan, Korea.
*These authors contributed equally to this work.
†Corresponding author. Email: zhao@unist.ac.kr

Here, we demonstrate the effect of state-dependent alignment on the scattering of CS_2 molecules by a standing wave formed by two counter-propagating pulsed infrared (IR) laser beams of identical properties: wavelength λ, waist radius (e^{-2} radius) w_0, pulse duration [full width at half maximum (FWHM)] τ, polarization, and peak intensity I_0. To investigate the alignment effect, we use rotationally cold molecules ($T_{rot} \sim 1$ K) occupying only a few rotational states. Control experiments are performed with molecules at $T_{rot} \sim 35$ K, where the alignment effect is predicted to be averaged out (23). The molecular beam of $T_{rot} \sim 1$ or 35 K is transversely dispersed by the optical standing wave. We measure the resulting velocity distributions using a velocity map imaging technique (39). The shape of the distribution varies drastically with increasing I_0. This effect is well reproduced by quantum classical simulations if these include the state-dependent alignment of the molecules. Our results therefore demonstrate how rotational state–specific alignment of molecules can be exploited to manipulate their translational motion. This illustrates that the rotational state–dependent force imparted by the nonresonant optical standing wave can be used as a new tool for rotational state selection of nonpolar molecules.

The interaction potential between the ground-state CS_2 molecules ($^1\Sigma$) and a laser field of intensity I is $U = -\frac{1}{2}(\alpha_{\parallel}\cos^2\theta + \alpha_{\perp}\sin^2\theta) Z_0 I = -\frac{1}{2}Z_0 I[(\alpha_{\parallel} - \alpha_{\perp})\cos^2\theta + \alpha_{\perp}]$, where $\alpha_{\parallel}$ and $\alpha_{\perp}$ are the polarizability components parallel and perpendicular to the molecular axis, θ is the polar angle between the molecular and laser polarization axes, and Z_0 is the vacuum impedance. Spherical harmonics $Y_{j,M} = |j,M\rangle$ and their superpositions $\Psi_{J,M}(I) = \sum_j C_j^{J,M}(I) \,|\, jM\rangle$ (2) describe the rotational motion of the molecules in the absence ($I = 0$) and presence ($I > 0$) of the field, respectively. Here, j and M are the quantum numbers respectively associated with the rotational angular momentum and its projection onto the laser polarization axis with j restricted to even integers for $^{12}C^{32}S_2$ (40). $\Psi_{J,M}$ evolves from $\Psi_{J,M}(I = 0) = |j,M\rangle$ to $\Psi_{J,M}(I)$ when the field is turned on slowly over a time scale longer than the rotational period (41).

The expectation value $\langle\Psi_{J,M}|\cos^2\theta|\Psi_{J,M}\rangle$ represents the state-dependent directional properties of molecules in a laser field and is known as the alignment cosine. The alignment cosine denoted by $\langle\cos^2\theta\rangle_{J,M} = \langle\cos^2\theta\rangle_{J,M}(I)$ is a rotational state–dependent function of the laser intensity. Thus, the polarizability component along the space-fixed laser polarization axis is $\alpha_{J,M}(I) = (\alpha_{\parallel} - \alpha_{\perp})\langle\cos^2\theta\rangle_{J,M} + \alpha_{\perp}$ (12). Since the time scale of the intensity variation associated with molecular translation generally surpasses the rotational period by several orders of magnitude (14), the classical trajectories of molecules or the quantum phase accumulated along the beam path in slowly varying laser fields is determined by the approximate potential $U_{J,M}(\mathbf{r},t) = -\frac{1}{2}\alpha_{J,M}[I(\mathbf{r},t)]I(\mathbf{r},t)Z_0$.

In Fig. 1B, we plot the calculated alignment cosine $\langle\cos^2\theta\rangle_{J,M}(I)$ and the corresponding $\alpha_{J,M}(I)$ for the lowest rotational states of $J = 0$ (black) and $J = 2$ (red, blue, and light orange) for an optical standing wave field characterized by the spatial intensity profile plotted in Fig. 1A. The deviation of $\alpha_{J,M}(I)$ from $\alpha_{J,M}(0)$ at $x = \pm0.25\lambda$ (at the standing wave nodes where the intensity vanishes) indicates the molecular alignment effect, as seen from the corresponding change of $\langle\cos^2\theta\rangle_{J,M}$. $\alpha_{J,M}(0)$ represents the polarizability without considering the alignment effect. Note that not only the maximum $\alpha_{J,M}(I)$ value but also the aspect of alignment depend on the rotational quantum state. Generally, $\alpha_{J,M}(I_{max}) > \alpha_{J,M}(0)$, except for the state of $J = 2$ and $M = 0$ at very small I. Only a small fraction of CS_2 molecules populates this state at $T_{rot} = 1$ K, and their contributions to the velocity profiles are less substantial.
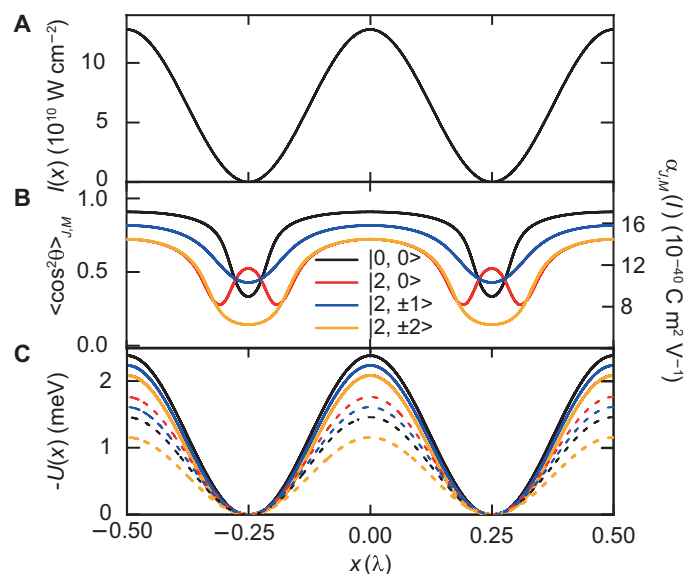

Fig. 1. State-dependent alignment-considering molecular polarizability $\alpha_{J,M}(I)$ and the corresponding molecular interaction potential for the given standing wave intensity variation. (**A**) Spatial intensity profile of an optical standing wave plotted as a function of x. The maximum intensity I_{max} of the standing wave is 13×10^{10} W/cm². (**B**) The estimated alignment cosine $\langle\cos^2\theta\rangle_{J,M}$ (left) and the corresponding molecular polarizability $\alpha_{J,M}[I(x)]$ (right) shown for the spatially varying field intensity and for rotational states of $J = 0$ (black) and 2 (red, blue, and light orange). These two J states account for 88% of the CS_2 population at $T_{rot} = 1$ K. (**C**) Molecular interaction potentials $U_{J,M}[I(x)]$ for $\alpha_{J,M}[I(x)]$ (solid lines) and $\alpha_{J,M}(0)$ (dotted lines) for the states marked in (B). The red solid curve is partially concealed by the light orange one.

The molecular interaction potentials $U_{J,M}[I(x)]$ are plotted for $\alpha_{J,M}[I(x)]$ (solid lines) and $\alpha_{J,M}(0)$ (dotted lines) in Fig. 1C. The molecular alignment strengthens the dipolar interaction and changes the order of $U_{J,M}(x = 0)$. For example, $|U_{J,M}(x = 0; \alpha_{J,M}[I(x)])| > |U_{J,M}(x = 0; \alpha_{J,M}[I = 0])|$ and $|U_{0,0}(x = 0)|$ and $|U_{2,0}(x = 0)|$ are, respectively, the largest with and without considering molecular alignment. Therefore, the state-dependent alignment needs to be considered for the proper analysis of experiments at low T_{rot}.

RESULTS

Figure 2 shows an illustration of our experiment [see (9) and Materials and Methods for details]. A rotationally cold molecular beam is collimated by two skimmers and a vertical slit before it interacts with the optical standing wave of intensity $I(x,y,z,t) = 4I_0\exp[-2(y^2 + z^2)/w_0^2]\exp.[-4\ln(2)(t/\tau)^2]\cos^2(2\pi x/\lambda)$, formed by two counter-propagating laser beams (IR1 and IR2). Their waist radius w_0 and pulse width τ are 21.5 ± 1.0 µm and 7.5 ± 0.1 ns, respectively. Only molecules that pass through the center of the standing wave and occupy the vibrational ground state are ionized by a probe dye laser beam (Probe) through resonance enhanced multiphoton ionization (REMPI) processes with the transition $[\frac{1}{2}]np\,\sigma_u(^1\Pi_u) \leftarrow \tilde{X}^1\Sigma_g^+$ (42, 43). An ion lens system consisting of three electrodes performs velocity map imaging, namely, ions with the same initial velocity are mapped onto the same position at the two-dimensional ion detector (39). The ion signal is amplified and converted into a light signal by a multichannel plate (MCP) and a phosphor screen (PS), respectively. The
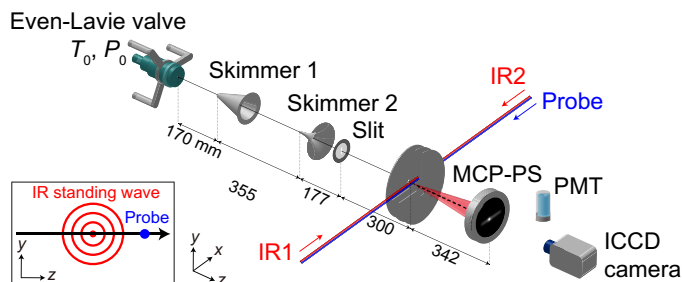
Fig. 2. Schematic diagram of the experimental setup. A molecular beam of CS_2 molecules is scattered by a pulsed optical standing wave. The rotationally cold molecular beam is produced by supersonic expansion from an Even-Lavie valve with stagnation pressure P_0 and temperature T_0. The standing wave is formed by focusing two counter-propagating laser beams (IR1 and IR2). Their wavelengths λ and waist radii w_0 are 1064 nm and 22 μm, respectively. The velocity change due to the scattering is measured by the velocity map imaging technique. We ionize molecules passing through the center of the standing wave by a probe dye laser beam (Probe). An ion lens system consisting of three electrodes performs velocity map imaging. The ion signal is amplified and converted into a light signal by an MCP and a PS, respectively. The luminescence is recorded by an ICCD camera and a PMT.

luminescence is recorded by an intensified charge-coupled device (ICCD) camera and a photomultiplier tube (PMT). The foci of IR1 and IR2 overlap at the origin of our coordinate system. IR1 propagates parallel to the positive x axis, while IR2 and Probe propagate in the opposite direction. The linear polarization axis of the three laser beams corresponds to the vertical direction, which we choose as the y axis. The molecular beam direction is almost parallel to the z axis with a deviation angle of 5 mrad.

Figures 3 and 4 show sets of measured (first panel) and simulated (second panel) velocity map images of CS_2 molecules scattered by the standing wave for $T_{rot} \sim 1$ or 35 K, respectively, with I_0 ranging from 0 to 6.3×10^{10} W/cm^2. The images show the transverse velocity distribution functions $f(v_x,v_y;I_0)$. In the third panel, we compare the velocity profiles along the v_x axis $h(v_x;I_0)$ of the two images.

Figures 3A and 4A present the velocity distributions $f(v_x,v_y)_{off} = f(v_x,v_y;I_0 = 0)$ and their profiles $h(v_x)_{off} = h(v;I_0 = 0)$ obtained with the standing wave off. $f(v_x,v_y)_{off}$ is a convolution of the initial transverse velocity distribution function with the velocity changes during ionization v_{recoil} and blurring at the detector. In our experiment, the detector blurring dominates $f(v_x,v_y)_{off}$. The simulated and measured data agree well except that the measured image and profile have wider tails than simulated counterparts. This difference might be due to the high peak intensity (about 10^{11} W/cm^2) of the probe laser. The detailed mechanisms of the dependence on the probe intensity are not yet fully understood.

The measured images and profiles vary drastically with increasing I_0 as shown in Figs. 3 (B to H) and 4 (B to H): Pairs of outer peaks appear sequentially, while the width and position of the central peak vary. The outer peaks are associated with rainbow-like singularities (15, 22), which are substantially suppressed by the detector blurring. In Fig. 3H, there exist shoulders at $v_x = 12$ and -29 m/s, which are manifestation of additional rainbow-like singularities and are absent in Fig. 4H. Also note that the dataset for $I_0 = 2.4 \times 10^{10}$ W/cm^2 in Fig. 3D is similar to the one for $I_0 = 3.2 \times 10^{10}$ W/cm^2 in Fig. 4E.

This is well reproduced by our simulations including state-dependent alignment. The deviation in Figs. 3 and 4 can be attributed to the same mechanisms related to the imperfect reproduction of measured off images in Figs. 3A and 4A and to the lateral fluctuation
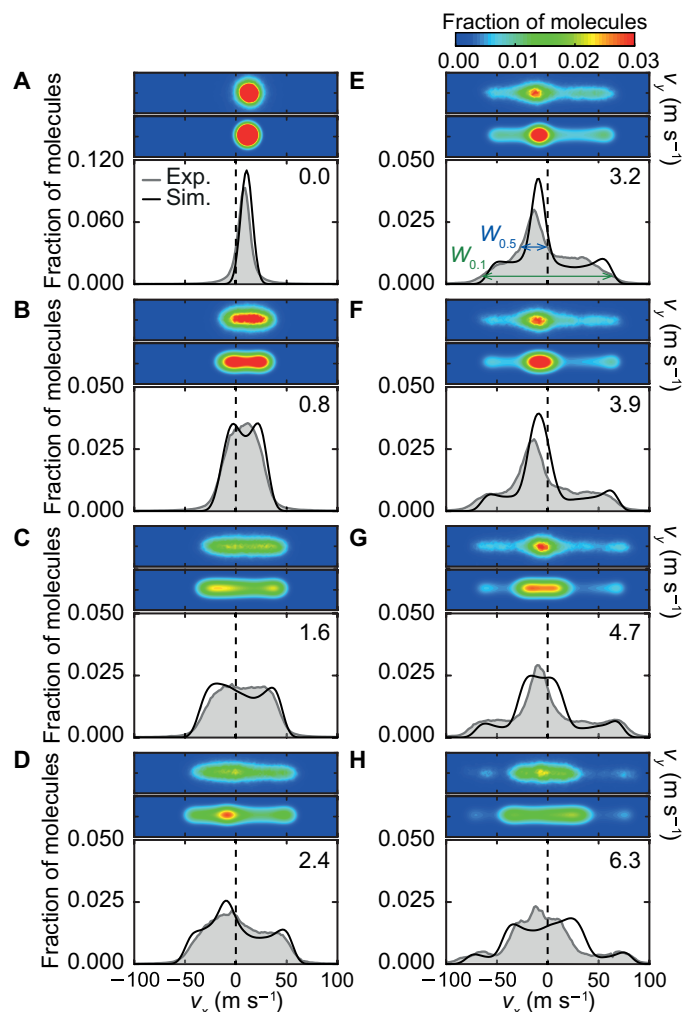

Fig. 3. The measured (first panel) and simulated (second panel) transverse velocity distributions and their profiles (third panel) along the v_x axis for eight I_0 values for $T_{rot} = 1$ K. (A to H) The number in each graph indicates I_0 in the unit of 10^{10} W/cm^2. The accumulation time for the measured images is 1200 s, which corresponds to 12,000 laser shots. The images are normalized to the total signal intensity of each image. Gray profiles with shading and solid black curves correspond to the profiles of the measured and simulated images, respectively. The profile in (A) represents the initial transverse velocity distribution, which is centered at $v_x \approx 10$ m/s. As I_0 increases, the profile becomes asymmetric and its central peak position moves to $v_x \approx -10$ m/s. These asymmetries result from the phase-space rotation of the molecules during the laser pulse duration and the average initial velocity along the x axis, $\langle v_{0x} \rangle \approx 10$ m/s (see Fig. 5, G and H, and Discussion for details). The degree of the rotation depends on $U_{J,M}(I) \propto \alpha_{J,M}(I)I$, which varies the asymmetries according to I_0. For an initial velocity distribution of $\langle v_{0x} \rangle = 0$, the profiles would be symmetric.

of the IR foci (SD, 2.9 μm). In the simulations, we use the $\langle v_{0x} \rangle$ value as a fitting parameter, determined as 10 ± 1 m/s, with other parameters predetermined in the previous experiment (T_{rot}) (9) or determined by deflection experiments with a single propagating laser beam (w_0). The details of the simulation can be found in Material and Methods.

In addition, simulated results using the alignment-ignored polarizability $\alpha_{J,M}(0)$ are compared with the experimental data. Figure 5A shows the measured and the two simulated velocity profiles for $I_0 = 3.2 \times 10^{10}$ W/cm^2. Dissimilar from the simulated profile with $\alpha_{J,M}(I)$,
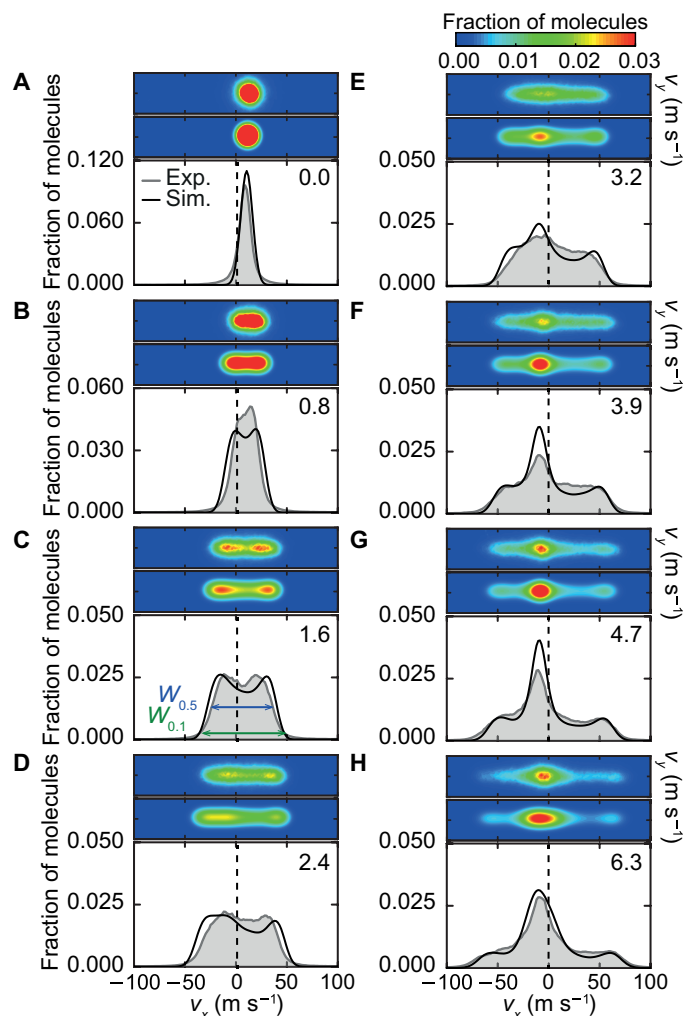
Fig. 4. The same data as Fig. 3 for T_{rot} = 35 K. (A to H) Compared with the data for T_{rot} = 1 K in Fig. 3, a distinctive central peak around v_x = −10 m/s appears at higher I_0 for T_{rot} = 35 K. This peak turns up in (F) at I_0 = 3.9 × 10^{10} W/cm^2, while it is clearly visible at I_0 = 3.2 × 10^{10} W/cm^2 for the lower rotational temperature (Fig. 3E). The shift of the peak arises from the half phase-space rotation of the initial distribution of the molecules. At T_{rot} = 35 K, average values of <cos^{2}θ>$_{J,M}$ and $α_{J,M}(I)$ are smaller than at T_{rot} = 1 K, as the molecules are less aligned at the higher temperature. Since the degree of the rotation increases with the product of $α_{J,M}(I)$ and I, the half rotation requires higher I for T_{rot} = 35 K.

Fig. 5. Comparison of the experimental measurements with two series of numerical simulation obtained with $α_{J,M}(I)$ and $α_{J,M}(0)$. (A) The measured velocity profile for I_0 = 3.2 × 10^{10} W/cm^2 (gray profile with shading) is plotted together with the corresponding simulated profiles obtained with (solid curve) and without (dashed curve) considering the molecular alignment. Two characteristic velocity widths, $W_{0.1}$ and $W_{0.5}$, are marked in the experimental profile (green and blue, respectively). **(B and C)** Velocity widths $W_{0.1}$ and $W_{0.5}$, determined from measured and simulated profiles, plotted against I_0 for T_{rot} = 1 K (B) and T_{rot} = 35 K (C). Squares denote measured data, while solid and dotted curves represent simulation data with $α_{J,M}(I)$ (considering alignment) and $α_{J,M}(0)$ (ignoring alignment), respectively. **(D)** Horizontal error bars are estimated from the nominal energy stability of an IR laser beam (0.8%) and uncertainties in w_0, τ, and pulse energy measurements (±0.1 mJ). Vertical error bars are calculated assuming ±10% errors in the profile peak determination. Calculated positions of molecules in the lowest rotational state (J = 0) are plotted as functions of time for 16 different trajectories, accounting for alignment effects [$α_{J,M}(I)$, solid curves]. For two representative position functions A and B, we show comparison curves A' and B' calculated without alignment effects [$α_{J,M}(0)$, dashed curves]. **(E and F)** The simulation results at t = 5 ns are plotted in phase-space diagrams for $α_{J,M}(I)$ (E) and $α_{J,M}(0)$ (F). The dotted curve indicates a separatrix at t = 0 ns, inside which the molecules are temporally trapped by the standing wave potential. Thick blue and green lines show two representative trajectories, corresponding to A and B in frame (D), from t = −5 to 5 ns [open circle at −5 ns, filled circle at 5 ns, compare to red shaded area in (D)]. The minimum $W_{0.5}$ in (B) is associated with the half phase-space rotation of the molecules near the center of the diagram in (E). For $α_{J,M}(0)$, those molecules cannot make a half rotation as illustrated by the three blue trajectories, resulting in a larger $W_{0.5}$. The larger v_x for B than for B' originates from the wider vertical width of the separatrix for $α_{J,M}(I)$ than for $α_{J,M}(0)$ and leads to the larger $W_{0.1}$.

the simulated profile with $α_{J,M}(0)$ is notably distinct from the measured one.

For a more quantitative comparison, we define two characteristic widths of the velocity distribution $h(v_x)_{on}$: $W_{0.5}$ and $W_{0.1}$. These widths indicate the velocity outer-full widths at 50 and 10% of the maximum, respectively. Despite the arbitrary choice of the two widths, $W_{0.5}$ and $W_{0.1}$ represent a good quantitative measure for the shape variation of $h(v_x)_{on}$ with I_0. In Fig. 5B, the two widths are plotted in different colors against I_0. The experimental data (symbols) are compared with the results calculated with $α_{J,M}(I)$ (solid lines) and $α_{J,M}(0)$ (dotted lines). The theoretical $W_{0.5}$ curves display a threshold I_0* value at which $W_{0.5}$ changes abruptly and exhibit a minimum at $I_{0,min}$. The effect of state-dependent molecular alignment is characterized

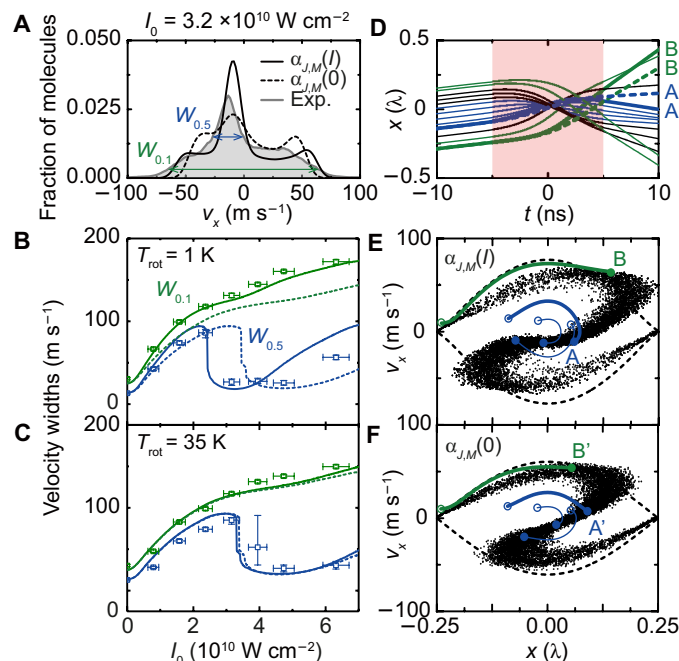by two aspects: (i) a decrease in I_0* and $I_{0,min}$ and (ii) an increase in $W_{0.1}$.

On the other hand, at the higher rotational temperature of T_{rot} = 35 K, the two corresponding simulation results are almost identical and agree well with the measurements (Fig. 5C), thereby confirming previous experimental results (*22*) and theoretical predictions (*23*) quantitatively. The agreement also validates the determination of <v_{0x}>.

DISCUSSION

The different dipolar potentials for the two cases shown in Fig. 1C are responsible for the dissimilar simulated profiles in Fig. 5A. The acceleration given by the optical dipole force $\mathbf{F} = -\nabla U$ determines molecular trajectories and final velocities. Figure 5D shows calculated molecular trajectories (solid curves) with $\alpha_{J,M}(I)$ for $I_0 = 3.2 \times 10^{10}$ W/cm^2 and initial conditions of $v_{0x} = 10$ m/s, $v_{0y} = 0$ m/s, $v_{0z} = 1740$ m/s, and $J = 0$. Two representative trajectories shown as thick solid curves (A and B) are compared with the corresponding ones simulated with $\alpha_{J,M}(0)$ (thick dashed curves, A′ and B′). The alignment effect leads to a large variation in molecular positions. The slopes of the corresponding pairs of solid and dashed curves at $t = 10$ ns, representing the calculated final velocities, appear to be substantially different.

The two aspects manifested in Fig. 5B can be understood qualitatively with the molecular dynamics in phase space. The two phase-space plots in Fig. 5 (E and F) show the calculated results at $t = 5$ ns with and without considering molecular alignment, respectively, together with the corresponding separatrices at $t = 0$ (dotted lines). Here, we neglect the effects of electron recoil and detector blurring. If the laser intensity I and the molecular polarizability α were constant, the time required for a half phase-space rotation, t_{half}, would be reversely proportional to $(4I\alpha)^{1/2}$ for molecules near the center of the diagram where the potential can be assumed to be harmonic. In other words, the extent of phase-space rotation for a given time increases with $(4I\alpha)^{1/2}$.

Although the standing wave is pulsed in our work, this proportionality still gives a qualitative understanding. Aspect (i), the decrease in I_0^* and $I_{0,min}$, is closely related to the condition at which $t_{half} = \tau$ (36, 37). For example, $t_{half} = 7.1$ ns at $I_0 = 3.2 \times 10^{10}$ W/cm^2, which is evaluated with $I = I_0$ and $\alpha = \langle\alpha_{J,M}(4I_0)\rangle$. Thus, the molecules near the center of the separatrix (blue trajectories in Fig. 5 (D and E)) have performed nearly a half rotation at $t = 5$ ns, as shown in Fig. 5E corresponding to the minimum of $W_{0.5}$. On the other hand, when the alignment effect is ignored, $t_{half} = 8.7$ ns and the corresponding molecules (blue trajectories in Fig. 5F) rotate quite less than 180° at the same conditions. The half rotation might occur at $I_{0,min} = 4.7 \times 10^{10}$ W/cm^2, which is quite close to $I_{0,min}$ of the dotted blue curve in Fig. 5B. Therefore, the half phase-space rotation during the laser pulse duration explains the rather distinctive peaks at $v_x \approx -10$ m/s of the profiles in Figs. 3 (E and F) and 4 (F to H). The underlying physics of the similar peak in Fig. 3 (G and H) is not clear at this moment. At least, these peaks are not caused by the detection of untrapped particles, to which strong peaks at an initial velocity or energy value was attributed in the previous scattering experiments (38, 44), since they are different from the initial peak position in Fig. 3A.

Aspect (ii), the increase in $W_{0.1}$, is associated with the molecules following anharmonic dynamics (45). The vertical width of the separatrix is proportional to $(4I\alpha)^{1/2}$, which determines the maximum $|v_x|$ of molecules near the separatrix where the anharmonicity of the potential plays a important role. Since, generally, $\alpha_{J,M}(4I_0) > \alpha_{J,M}(0)$, the alignment-considered analysis always shows a larger $W_{0.1}$ than the alignment-ignored analysis.

The rotational temperature dependence in the transverse velocity distributions affects the degree of phase-space rotation and the increase in the outer width, both of which are proportional to $(4I\alpha)^{1/2}$. Since the state-averaged $\alpha_{J,M}(4I)$ is bigger for $T_{rot} = 1$ K than for $T_{rot} = 35$ K, stronger I_0 is necessary for $T_{rot} = 35$ K to attain the similar phase-space rotation and outer width for $T_{rot} = 1$ K. This explains the

resemblance between Figs. 3D and 4E. The distance between inner rainbow-like peaks also scales with $(4I\alpha)^{1/2}$, which, together with the narrow distribution of rotational states at $T_{rot} = 1$ K, accounts for the distinctive shoulders in Fig. 3H. At $T_{rot} = 35$ K, the molecules occupy a large number of rotational states. The distance between the rainbow-like peak pair varies with the rotational state, and the maximum distance is smaller for the higher rotational temperature. Therefore, the weak rainbow-like feature spreads out, and it is not visible in Fig. 4H (22).

Overall, for $T_{rot} = 1$ K, the simulation based on $\alpha_{J,M}(I)$ shows much better agreement with the experimental data than the one based on $\alpha_{J,M}(0)$. This agreement confirms the effect of state-dependent molecular alignment on molecular scattering by an optical standing wave.

Our demonstration has implications for various experimental studies on both coherent and incoherent scattering of molecules in directional states by optical standing waves. Our experiment can serve as a new tool for measuring the polarizability anisotropy $\Delta\alpha = \alpha_\parallel - \alpha_\perp$ of small molecules. The alignment cosine depends on anisotropy, as does the interaction potential. Therefore, the molecular polarizability anisotropy could be measured by comparing widths of measured and simulated profiles as shown in Fig. 5 (B and C), with other parameters such as a rotational temperature of predetermined samples. Such a method for measuring the polarizability anisotropy is complementary to the techniques based solely on the molecular alignment by nonresonant propagating laser fields (46–49).

Furthermore, scattering from a nonresonant optical standing wave can be applied to achieve rotational state selection of nonpolar molecules, complementing recently demonstrated techniques for state selection of polar molecules (50, 51). According to our analysis considering the alignment effect, the velocity profile of Fig. 3B implies that the part of $v_x < -17.4$ m/s (about 2.1% of the total area) contains molecules in the $J = 0$ state with a purity of 95%. The fraction and purity can be improved further by optimizing parameters such as I_0, w_0, τ, $\langle v_{0x}\rangle$, and T_{rot}. For example, the fraction and the purity for the part of $v_x < -29.9$ m/s are 3.2 and 95.4%, respectively, in the simulation using $I_0 = 1.16 \times 10^{10}$ W/cm^2, $w_0 = 80$ μm, $\tau = 28$ ns, and $\langle v_{0x}\rangle = 30$ m/s (see fig. S2). These parameters are feasible with current technology (28). Furthermore, a larger w_0 makes this method more robust, because the lateral fluctuations of the IR foci (about 3 μm) get less influential with increasing w_0. Note that state-dependent alignment is critical not only in state-selection studies but also in state-dependent deceleration of molecules of low rotational temperature with moving lattice potentials (37, 38), where an analysis neglecting the state-dependent alignment will lead to incorrect results.

Although our present analysis concerns CS$_2$, the rotational state selection by an optical standing wave can be applied more broadly. Since the acceleration of two adjacent rotational states differs by the order of $(\Delta\alpha B/I)^{1/2}/m$ (10), the selection of the rotational ground state $J = 0$ can be easily implemented for all linear molecules with sufficiently large rotational constant B or small mass m. Further studies are required to test the applicability of this method to larger molecules, symmetric tops or asymmetric tops, and rotational states of $J > 0$. However, the effect of the state-dependent alignment will be critical for all these studies.

Last, we note that the degree of molecular alignment can be fine-tuned to some extent by varying the standing wave's polarization state. For instance, an optical standing wave formed by two counter-rotating elliptically polarized light beams with ellipticity ε and intensity of $(1 + \epsilon^2)I_0$ exhibits linear polarization rotating periodically

along the x axis, while its intensity profile is given by $I(x) = 2I_0[(1 + \epsilon^2) + (1 - \epsilon^2)\cos(4\pi x/\lambda)]$ (52). Thus, varying ϵ makes it possible to adjust the minimum intensity $4I_0\epsilon^2 > 0$, thereby allowing control of the degree of molecular alignment in the standing wave field.

The state-dependent directional properties of molecules are important in controlling translational molecular motions in various combinations of optical standing waves, electric, and magnetic fields. As well as the interaction of polarizable molecules with an optical field, it is known that interaction of polar molecules with combined optical and electric fields depends on their directional properties. Angular motions of molecules in such combined fields have been studied theoretically (53, 54) and experimentally (55, 56) for propagating laser fields. It will be intriguing to extend these studies toward controlling molecular translation using standing wave fields.

MATERIALS AND METHODS
Experimental design
The apparatus operating at 10-Hz repetition rate is the same as the one used in our previous work (9), except optical standing waves replace propagating waves. A pulsed cold molecular beam is produced by expanding CS_2 molecules at 427 mbar, which is the CS_2 vapor pressure at 295 K, in 21 or 81 bar of He carrier gas through an Even-Lavie valve into high vacuum. Under these source conditions, the respective high-vacuum pressures in the source chamber are 3.9×10^{-7} and 1.1×10^{-6} mbar, respectively. The resulting rotational temperatures T_{rot} were estimated to be 1 and 35 K, respectively, in the previous report (9). The molecular beam is collimated by two skimmers (Skimmer1 and Skimmer2) of 3- and 1-mm diameter, respectively. The second chamber is located between the two skimmers. Skimmer2 separates the second chamber and the detection chamber. The pressures of the two chambers are below 3.0×10^{-8} mbar. A vertical slit of 200-μm width and 3-mm height further collimates the molecular beam along the x axis. The collimated molecular beam is crossed at 89.7° by a pulsed standing wave. All the distances between the components are given in Fig. 2.

Two counter-propagating laser pulses (IR1 and IR2) with the same properties overlap at the center of the detection chamber to form the pulsed standing wave. A single pulse from an injection-seeded Nd:YAG laser, whose wavelength λ and pulse width τ are 1064 nm and 7.5 ± 0.1 ns (FWHM), respectively, passes through an optical isolator and is split into two by a beam splitter. After the beam splitter, the energy and polarization of the two pulses are adjusted by two sets of a zero-order half-wave plate and a Glan laser polarizer, respectively, to achieve the same peak intensity I_0 and linear polarization along the y axis. After propagating the same distance, they are focused by two lenses with focal lengths of 18.0 cm mounted on the opposite sides of the detection chamber. The waist radii w_0 of the focused laser beams are estimated as 21.5 ± 1.0 μm.

The molecules affected by the pulsed standing wave are ionized by a linearly polarized probe pulse of $\tau_{probe} = 4$ ns and $\lambda_{probe} = 477.7$ nm. At this wavelength, ionization occurs through a (3 + 1) REMPI process with the transition $\left[\frac{1}{2}\right] np\, \sigma_u(^1\Pi_u) \leftarrow \widetilde{X}\,^1\Sigma_g^+$ (42, 43). The probe pulse is produced by a dye laser pumped by a third harmonic of another Nd:YAG laser, of which the energy and polarization are set to 1.0 mJ and vertical polarization by a zero-order half-wave plate and a Glan laser polarizer. After being expanded by a set of a concave and convex lenses, the beam is focused by the same plano-convex lens that is used to focus IR2, which results in its waist radius $w_{0,probe}$

~ 5 μm. The probe pulse is delayed by 30 ns with respect to the IR pulses to avoid any two-color processes. The delay then requires a spatial shift of the dye focus along the z axis for the selected ionization of the dispersed molecules. To detect the most dispersed molecules, the y position of dye focal point is adjusted to $y = 0$.

The molecular ions are accelerated and focused by an electrostatic lens system onto a multi-channel plate (MCP) after flying 342 mm through a time-of-flight (TOF) tube. A repeller, an extractor, and ground electrodes made out of stainless steel constitute the ion lens system. They are 2-mm-thick disks of 90-mm diameter with holes at their center, whose diameters are 4 mm for the repeller and 20 mm for the others. The extractor is separated from the repeller and the ground by 16 mm. The voltages of the repeller and extractor are set to 900 and 644 V, respectively, which provide the velocity map imaging condition. Then, the ratio of the position at the detector to the TOF of an ion is its transverse velocity just after the ionization of a neutral molecule. This velocity is assumed to be the same as the velocity of the neutral molecule.

The ion signals are amplified and converted into luminescence by an MCP and a PS at its backside, respectively. The light signal from the PS is simultaneously detected and converted into electric signals by a PMT and an ICCD camera. The signals from the PMT and ICCD are transferred to a digital oscilloscope and a personal computer, respectively. We monitor the TOF spectrum on the scope to gate the intensifier, which allows us to record images of CS_2^+.

Velocity calculation
For the quantitative comparison of experimental and simulated data, we include the effect of the detector blurring in the calculation. The blurring at the MCP, the PS, and the intensifier constitute the total detector blurring function $g(v_x, v_y)_{detector}$. To quantify it, we analyze the smallest ion images with the number and intensity of the laser pulses set to minimal values. We fit a two-dimensional Gaussian function to each of those images. The average FWHMs along the x and y axes of the resulting Gaussian functions are 12.9 ± 1.5 and 13.3 ± 1.5 m/s, respectively. We approximate $g(v_x, v_y)_{detector}$ to a two-dimensional Gaussian function with these two FWHMs, $\Delta v_x^{detector}$ and $\Delta v_y^{detector}$.

To simulate $f(v_x, v_y)_{off}$ in the second panel in Figs. 3A and 4A, we approximate the initial velocity distribution function $g(v_{0x}, v_{0y})_{init}$ to a two-dimensional Gaussian function centered at ($<v_{0x}> = 10$ m/s, $<v_{0y}> = 0$ m/s) with the FWHMs $\Delta v_{0x} = 4.3$ and $\Delta v_{0y} = 3.6$ m/s, assume isotropic electron recoil during ionization, and use $g(v_x, v_y)_{detector}$ for the blurring at the detector. Δv_{0x} and Δv_{0y} are approximately determined from the line-of-sight argument. The given REMPI process results in $v_{recoil} = 2.7$ m/s (8). Since the spreads of $g(v_x, v_y)_{detector}$ are much larger than the other two factors, the detector blurring governs $f(v_x, v_y)_{off}$.

The Monte Carlo sampling method is used to select the initial velocity (v_{0x}, v_{0y}, v_{0z}), the initial position (x_0, y_0, z_0), and the initial rotational state $|j, M>$ of each individual molecule. Initial transverse velocities are given by $g(v_{0x}, v_{0y})_{init}$. The probability function for v_{0z} is a Gaussian function with the most probable velocity v_{mp} of 1740 m/s and an FWHM of 174 m/s. We determine z_0 from v_{0z} according to the following equation: $z_0 = v_{mp}t_{detection} - v_{0z}t_{simul}$. Here, $t_{detection}$ and t_{simul} are the detection and total simulation times, respectively. From this initial point, the individual molecule arrives at the detection plane $z = v_{mp}t_{detection}$ at $t = t_{detection}$. x_0 and y_0 are chosen randomly from a 200-μm-long line and a Gaussian distribution with a 2.9-μm-wide

FWHM, respectively. The FWHM of the Gaussian function is decided by considering $w_{0,probe}$ and the (3 + 1) REMPI process. The initial rotational state follows the Boltzmann distribution $e^{-Bj(j+1)/kT_{rot}}/q_r$, where k is the Boltzmann's constant and q_r is the rotational partition function.

For the given standing wave intensity, the dipolar potential is

$$U_{J,M}(x, y, z, t) = -2\alpha_{J,M}\left[I(x, y, z, t)\right]Z_0 I_0 \exp\left[\frac{-2(y^2 + z^2)}{w_0^2}\right]\exp\left(-4\ln(2)\frac{t^2}{\tau^2}\right)\cos^2\left(\frac{2\pi}{\lambda}x\right).$$

With the optical dipole force $\mathbf{F}_{J,M}(x, y, z, t) = -\nabla U_{J,M}(x, y, z, t)$ exerted on a molecule of mass m, we calculate the velocity change of molecules passing through the standing wave $\delta v_i = v_i - v_{i0} = \int \frac{1}{m} F_{i,J,M}(x, y, z, t) \, dt (i = x, y, z)$.

By collecting 20,000 trajectory calculation results, $v_i = v_{0i} + \delta v_i$ ($i = x, y, z$), we obtain the transverse velocity distribution function $g(v_x, v_y)_{on}$. In the velocity width calculations for $T_{rot} = 1$ K (35 K), trajectories of 100,000 molecules are used for 1.5×10^{10} W/cm$^2 < I_0 < 3.0 \times 10^{10}$ W/cm^2 (2.0×10^{10} W/cm$^2 < I_0 < 2.8 \times 10^{10}$ W/cm^2 and 3.4×10^{10} W/cm$^2 < I_0 < 3.6 \times 10^{10}$ W/cm^2), the intensity ranges where the velocity widths change abruptly, to reduce the fluctuation in the values due to insufficient statistical average. With the standing wave field off, the corresponding distribution $g(v_x, v_y)_{off}$ is equal to the initial transverse velocity distribution function $g(v_{0x}, v_{0y})_{init}$.

The final velocity distribution functions $f(v_x, v_y)_{on}$ and $f(v_x, v_y)_{off}$ are the respective convoluted functions of $g(v_x, v_y)_{on}$ and $g(v_x, v_y)_{off}$ with $g(v_x, v_y)_{ionization}$ and $g(v_x, v_y)_{detector}$. $g(v_x, v_y)_{ionization}$ originates from the velocity change v_{recoil} induced by electron recoil during ionization. If spherical symmetric ionization is assumed, the resulting velocity distribution forms a thin spherical shell, $v_x^2 + v_y^2 + v_z^2 = v_{recoil}^2$. Then, $g(v_x, v_y)_{ionization}$ is the projection of the sphere distribution on the detection plane.

SUPPLEMENTARY MATERIALS

Supplementary material for this article is available at http://advances.sciencemag.org/cgi/content/full/6/14/eaaz0682/DC1

REFERENCES AND NOTES

1. H. Stapelfeldt, T. Seideman, *Colloquium*: Aligning molecules with strong laser pulses. *Rev. Mod. Phys.* **75**, 543–557 (2003).
2. M. Lemeshko, R. V. Krems, J. M. Doyle, S. Kais, Manipulation of molecules with electromagnetic fields. *Mol. Phys.* **111**, 1648–1682 (2013).
3. J. Küpper, S. Stern, L. Holmegaard, F. Filsinger, A. Rouzée, A. Rudenko, P. Johnsson, A. V. Martin, M. Adolph, A. Aquila, S. Bajt, A. Barty, C. Bostedt, J. Bozek, C. Caleman, R. Coffee, N. Coppola, T. Delmas, S. Epp, B. Erk, L. Foucar, T. Gorkhover, L. Gumprecht, A. Hartmann, R. Hartmann, G. Hauser, P. Holl, A. Hömke, N. Kimmel, F. Krasniqi, K.-U. Kühnel, J. Maurer, M. Messerschmidt, R. Moshammer, C. Reich, B. Rudek, R. Santra, I. Schlichting, C. Schmidt, S. Schorb, J. Schulz, H. Soltau, J. C. H. Spence, D. Starodub, L. Strüder, J. Thøgersen, M. J. J. Vrakking, G. Weidenspointner, T. A. White, C. Wunderer, G. Meijer, J. Ullrich, H. Stapelfeldt, D. Rolles, H. N. Chapman, X-Ray diffraction from isolated and strongly aligned gas-phase molecules with a free-electron laser. *Phys. Rev. Lett.* **112**, 083002 (2014).
4. C. J. Hensley, J. Yang, M. Centurion, Imaging of isolated molecules with ultrafast electron pulses. *Phys. Rev. Lett.* **109**, 133202 (2012).
5. R. Li, P. Liu, P. Wei, Y. Li, S. Zhao, Z. Zeng, Z. Xu, in *Progress in Ultrafast Intense Laser Science VII*, K. Yamanouchi, D. Charalambidis, D. Normand, Eds. (Springer Berlin Heidelberg, 2011), chap. 6, pp. 127–143.
6. J. Itatani, J. Levesque, D. Zeidler, H. Niikura, H. Pépin, J. C. Kieffer, P. B. Corkum, D. M. Villeneuve, Tomographic imaging of molecular orbitals. *Nature* **432**, 867–871 (2004).
7. S. M. Purcell, P. F. Barker, Tailoring the optical dipole force for molecules by field-induced alignment. *Phys. Rev. Lett.* **103**, 153001 (2009).
8. S. M. Purcell, P. F. Barker, Controlling the optical dipole force for molecules with field-induced alignment. *Phys. Rev. A* **82**, 033433 (2010).
9. X. N. Sun, B. G. Jin, L. Y. Kim, B. J. Kim, B. S. Zhao, Strong optical dipole force exerted on molecules having low rotational temperature. *Chem. Phys. Chem.* **17**, 3701–3708 (2016).
10. B. Friedrich, D. Herschbach, Alignment and trapping of molecules in intense laser fields. *Phys. Rev. Lett.* **74**, 4623–4626 (1995).
11. B. Friedrich, D. Herschbach, Polarization of molecules induced by intense nonresonant laser fields. *J. Phys. Chem. A* **99**, 15686–15693 (1995).
12. T. Seideman, Shaping molecular beams with intense light. *J. Chem. Phys.* **107**, 10420–10429 (1997).
13. T. Seideman, Molecular optics in an intense laser field: A route to nanoscale material design. *Phys. Rev. A* **56**, R17–R20 (1997).
14. T. Seideman, Manipulating external degrees of freedom with intense light: Laser focusing and trapping of molecules. *J. Chem. Phys.* **106**, 2881–2892 (1997).
15. E. Gershnabel, I. S. Averbukh, Deflection of field-free aligned molecules. *Phys. Rev. Lett.* **104**, 153001 (2010).
16. E. Gershnabel, I. S. Averbukh, Controlling molecular scattering by laser-induced field-free alignment. *Phys. Rev. A* **82**, 033401 (2010).
17. H. Stapelfeldt, H. Sakai, E. Constant, P. B. Corkum, Deflection of neutral molecules using the nonresonant dipole force. *Phys. Rev. Lett.* **79**, 2787–2790 (1997).
18. B. S. Zhao, H. S. Chung, K. Cho, S. H. Lee, S. Hwang, J. Yu, Y. H. Ahn, J. Y. Sohn, D. S. Kim, W. K. Kang, D. S. Chung, Molecular lens of the nonresonant dipole force. *Phys. Rev. Lett.* **85**, 2705–2708 (2000).
19. H. S. Chung, B. S. Zhao, S. H. Lee, S. Hwang, K. Cho, S.-H. Shim, S.-M. Lim, W. K. Kang, D. S. Chung, Molecular lens applied to benzene and carbon disulfide molecular beams. *J. Chem. Phys.* **114**, 8293–8302 (2001).
20. B. S. Zhao, S. H. Lee, H. S. Chung, S. Hwang, W. K. Kang, B. Friedrich, D. S. Chung, Separation of a benzene and nitric oxide mixture by a molecule prism. *J. Chem. Phys.* **119**, 8905–8909 (2003).
21. R. Fulton, A. I. Bishop, P. F. Barker, Optical Stark decelerator for molecules. *Phys. Rev. Lett.* **93**, 243004 (2004).
22. X. N. Sun, L. Y. Kim, B. S. Zhao, D. S. Chung, Rotational-state-dependent dispersion of molecules by pulsed optical standing waves. *Phys. Rev. Lett.* **115**, 223001 (2015).
23. L. Y. Kim, J. H. Lee, H. A. Kim, S. K. Kwak, B. Friedrich, B. S. Zhao, Effect of rotational-state-dependent molecular alignment on the optical dipole force. *Phys. Rev. A* **94**, 013428 (2016).
24. P. L. Kapitza, P. A. M. Dirac, The reflection of electrons from standing light waves. *Proc. Camb. Phil. Soc.* **29**, 297–300 (1933).
25. P. E. Moskowitz, P. L. Gould, S. R. Atlas, D. E. Pritchard, Diffraction of an atomic beam by standing-wave radiation. *Phys. Rev. Lett.* **51**, 370–373 (1983).
26. D. L. Freimund, K. Aflatooni, H. Batelaan, Observation of the Kapitza–Dirac effect. *Nature* **413**, 142–143 (2001).
27. M. A. Kadar-Kallen, K. D. Bonin, Light-force technique for measuring polarizabilities. *Phys. Rev. Lett.* **68**, 2015–2018 (1992).
28. C. Maher-McWilliams, P. Douglas, P. F. Barker, Laser-driven acceleration of neutral particles. *Nat. Photon.* **6**, 386–390 (2012).
29. O. Nairz, B. Brezger, M. Arndt, A. Zeilinger, Diffraction of complex molecules by structures made of light. *Phys. Rev. Lett.* **87**, 160401 (2001).
30. S. Gerlich, L. Hackermüller, K. Hornberger, A. Stibor, H. Ulbricht, M. Gring, F. Goldfarb, T. Savas, M. Müri, M. Mayor, M. Arndt, A Kapitza–Dirac–Talbot–Lau interferometer for highly polarizable molecules. *Nat. Phys.* **3**, 711–715 (2007).
31. S. Gerlich, M. Gring, H. Ulbricht, K. Hornberger, J. Tüxen, M. Mayor, M. Arndt, Matter-wave metrology as a complementary tool for mass spectrometry. *Angew. Chem. Int. Ed.* **47**, 6195–6198 (2008).
32. L. Mairhofer, S. Eibenberger, J. P. Cotter, M. Romirer, A. Shayeghi, M. Arndt, Quantum-assisted metrology of neutral vitamins in the gas phase. *Angew. Chem. Int. Ed.* **56**, 10947–10951 (2017).
33. J. Ramirez-Serrano, K. E. Strecker, D. W. Chandler, Modification of the velocity distribution of H_2 molecules in a supersonic beam by intense pulsed optical gradients. *Phys. Chem. Chem. Phys.* **8**, 2985–2989 (2006).
34. P. F. Barker, M. N. Shneider, Optical microlinear accelerator for molecules and atoms. *Phys. Rev. A* **64**, 033408 (2001).
35. P. F. Barker, M. N. Shneider, Slowing molecules by optical microlinear deceleration. *Phys. Rev. A* **66**, 065402 (2002).
36. G. Dong, W. Lu, P. F. Barker, Decelerating and bunching molecules with pulsed traveling optical lattices. *Phys. Rev. A* **69**, 013409 (2004).
37. R. Fulton, A. I. Bishop, M. N. Shneider, P. F. Barker, Controlling the motion of cold molecules with deep periodic optical potentials. *Nat. Phys.* **2**, 465–468 (2006).
38. A. I. Bishop, L. Wang, P. F. Barker, Creating cold stationary molecular gases by optical Stark deceleration. *New J. Phys.* **12**, 073028 (2010).
39. A. T. J. B. Eppink, D. H. Parker, Velocity map imaging of ions and electrons using electrostatic lenses: Application in photoelectron and photofragment ion imaging of molecular oxygen. *Rev. Sci. Instrum.* **68**, 3477–3484 (1997).

40. R. Torres, R. de Nalda, J. P. Marangos, Dynamics of laser-induced molecular alignment in the impulsive and adiabatic regimes: A direct comparison. *Phys. Rev. A* **72**, 023420 (2005).

41. L. Cai, J. Marango, B. Friedrich, Time-dependent alignment and orientation of molecules in combined electrostatic and pulsed nonresonant laser fields. *Phys. Rev. Lett.* **86**, 775–778 (2001).

42. J. Baker, M. Konstantaki, S. Couris, A resonance-enhanced multiphoton ionization study of the CS_2 molecule: The 4p Rydberg states. *J. Chem. Phys.* **103**, 2436–2444 (1995).

43. R. A. Morgan, M. A. Baldwin, A. J. Orr-Ewing, M. N. R. Ashfold, W. J. Buma, J. B. Milan, C. A. deLange, Resonance enhanced multiphoton ionization spectroscopy of carbon disulphide. *J. Chem. Phys.* **104**, 6117–6129 (1996).

44. M. Kozák, T. Eckstein, N. Schönenberger, P. Hommelhoff, Inelastic ponderomotive scattering of electrons at a high-intensity optical travelling wave in vacuum. *Nat. Phys.* **14**, 121–126 (2018).

45. H. L. Bethlem, G. Berden, A. J. A. van Roij, F. M. H. Crompvoets, G. Meijer, Trapping neutral molecules in a traveling potential well. *Phys. Rev. Lett.* **84**, 5744–5747 (2000).

46. S. Minemoto, H. Tanji, H. Sakai, Polarizability anisotropies of rare gas van der Waals dimers studied by laser-induced molecular alignment. *J. Chem. Phys.* **119**, 7737–7740 (2003).

47. D. Pinkham, T. Vogt, R. R. Jones, Extracting the polarizability anisotropy from the transient alignment of HBr. *J. Chem. Phys.* **129**, 064307 (2008).

48. S. Minemoto, H. Sakai, Measuring polarizability anisotropies of rare gas diatomic molecules by laser-induced molecular alignment technique. *J. Chem. Phys.* **134**, 214305 (2011).

49. H. Li, W. X. Li, Y. H. Feng, J. Liu, H. F. Pan, H. P. Zeng, Measurement of molecular polarizability anisotropy via alignment-induced spatial focusing and defocusing. *Phys. Rev. A* **85**, 052515 (2012).

50. S. Y. T. van de Meerakker, H. L. Bethlem, N. Vanhaecke, G. Meijer, Manipulation and control of molecular beams. *Chem. Rev.* **112**, 4828–4878 (2012).

51. Y.-P. Chang, D. A. Horke, S. Trippel, J. Küpper, Spatially-controlled complex molecules and their applications. *Int. Rev. Phys. Chem.* **34**, 557–590 (2015).

52. S. Eilzer, H. Zimmermann, U. Eichmann, Strong-field Kapitza-Dirac scattering of neutral atoms. *Phys. Rev. Lett.* **112**, 113001 (2014).

53. B. Friedrich, D. Herschbach, Enhanced orientation of polar molecules by combined electrostatic and nonresonant induced dipole forces. *J. Chem. Phys.* **111**, 6157–6160 (1999).

54. K. Sharma, B. Friedrich, Directional properties of polar paramagnetic molecules subject to congruent electric, magnetic and optical fields. *New J. Phys.* **17**, 045017 (2015).

55. H. Sakai, S. Minemoto, H. Nanjo, H. Tanji, T. Suzuki, Controlling the orientation of polar molecules with combined electrostatic and pulsed, nonresonant laser fields. *Phys. Rev. Lett.* **90**, 083001 (2003).

56. J. H. Nielsen, H. Stapelfeldt, J. Küpper, B. Friedrich, J. J. Omiste, R. González-Férez, Making the best of mixed-field orientation of polar molecules: A recipe for achieving adiabatic dynamics in an electrostatic field combined with laser pulses. *Phys. Rev. Lett.* **108**, 193001 (2012).